RSC Advances

PAPER

View Article Online
View Journal | View Issue

Cite this: *RSC Adv.*, 2025, **15**, 44508

Modulating phase composition and crystallization of 2D Ruddlesden–Popper perovskite films *via* a polyvinylidene fluoride buried interface

Juan Meng,[ab] Qiyou Lai,[a] Jingwen Li,[a] Sen Yang,[a] Chunying Wei,[a] Jiaqing Huang,[ab] Qi Lan,[ab] Leilei Yang, *[ab] Di Huang *[c] and André D. Taylor[d]

Uncontrolled crystallization and phase distribution remain major challenges in two-dimensional (2D) Ruddlesden–Popper (RP) perovskite films, often leading to the formation of undesirable small-*n* phases, poor out-of-plane orientation, and high defect density. Although polymer interlayers have been applied to improve film morphology, the underlying mechanisms and their effectiveness in quasi-2D systems remain insufficiently clarified. In this study, we present an effective interfacial engineering strategy to control phase distribution in two-dimensional (2D) Ruddlesden–Popper (RP) perovskite by incorporating an ultra-thin polyvinylidene fluoride (PVDF) interlayer at the buried interface. Comprehensive characterization reveals that the PVDF-modified interface significantly suppresses the formation of low-*n* ($n < 4$) phases in $BA_2MA_3Pb_4I_{13}$ perovskite films while promoting preferential out-of-plane orientation and enhanced crystallinity. The optimized devices with enhanced film morphology and phase purity lead to improved charge transport properties compared to the control devices fabricated directly on PEDOT:PSS. As a result, the PVDF-modified 2D RP perovskite solar cells achieve a champion power conversion efficiency of 11.03%, representing a 17.47% enhancement over reference devices without interfacial modification.

Received 26th August 2025
Accepted 10th November 2025

DOI: 10.1039/d5ra06360d

rsc.li/rsc-advances

Introduction

Two-dimensional Ruddlesden–Popper phase perovskite solar cells (2D RP PSCs) have gained significant attention as promising light-harvesting materials due to their outstanding optoelectronic properties and superior environmental stability.[1–4] Among them, $BA_2MA_3Pb_4I_{13}$ ($n = 4$) was chosen as the representative 2D Ruddlesden–Popper perovskite because it exhibits a moderate optical bandgap of approximately 1.63 eV, which is favorable for visible light absorption, and reduced exciton binding energy that facilitates efficient carrier transport.[5] Meanwhile, its layered structure with hydrophobic BA^+ spacers significantly improves environmental stability compared to 3D $MAPbI_3$ perovskites. Moreover, $n = 4$ compositions show excellent film forming ability, under certain conditions they can yield compact, highly oriented grains with low defect density, which are advantageous for device performance.[6] However, the uncontrolled nucleation and crystallization of 2D RP perovskite films frequently lead to several unresolved issues, including the excessive formation of small-*n* phases ($n < 4$) and random crystal orientation. For instance, even when the precursor composition is stoichiometrically designed for $n = 4$, the resulting films often contain mixed phases (*e.g.*, $n = 2$ and $n = 3$).[7,8] These small-*n* phases, possessing wider bandgaps, can act as recombination centers, which hampers efficient vertical charge transport. These limitations severely restrict performance of 2D RP PSCs.[9,10]

Recent efforts to address these challenges have focused on interfacial engineering strategies, such as introducing polymers or buffer layers at charge transport interfaces. Buried interface modification has emerged as an effective strategy to regulate the growth and crystallization of perovskite films, ultimately influencing the overall device performance.[11–15] Xie *et al.* investigated the role of the underlying hole-transport layer (HTL) wettability in the crystallization of 2D perovskite films by comparing hydrophilic poly(3,4-ethylenedioxythiophene):polystyrene sulfonate (PEDOT:PSS), moderately hydrophobic poly[bis(4-phenyl)(2,4,6-trimethylphenyl)amine] (PTAA), and highly hydrophobic poly(3-hexylthiophene-2,5-diyl) (P3HT).[16] Their findings revealed that moderately hydrophobic PTAA facilitated the formation of compact and uniform perovskite films with enhanced crystallinity. Beyond film morphology, the buried interface also plays a critical role in determining the phase composition and distribution within quasi-2D perovskite active

[a]*School of Physics and Electronic Information, Guangxi Minzu University, Nanning, 530006, China*

[b]*University Engineering Research Center of Multi-modal Information Intelligent Sensing, Processing and Application of Guangxi, Nanning, 530006, China*

[c]*Hunan University of Technology, Zhuzhou, 412008, China*

[d]*Department of Chemical and Biomolecular Engineering, Tandon School of Engineering, New York University, New York, NY 11201, USA*

layers. Otherwise, Tian *et al.* introduced an ultrathin PFN interlayer (<5 nm) to modify the PTAA surface, which effectively suppressed the formation of the $n = 1$ phase in 2D perovskite films.[17] This optimization led to improved light absorption of perovskite and achieved a power conversion efficiency (PCE) of 12.78% in $PEA_2MA_{3.5}FA_{0.5}Pb_5I_{16}$ ($n = 5$)-based solar cells. Similarly, Liu *et al.* demonstrated that a self-assembled monolayer of 4-bromobenzenediazonium tetrafluoroborate on PEDOT:PSS could induce a vertical phase gradient in perovskite films. While these methods have demonstrated improvements in morphology and device performance,[18] the mechanistic origin of performance enhancements remains ambiguous. In particular, it is not yet clear whether the improvements stem primarily from surface energy regulation, defect passivation, or moisture protection, and how these effects interplay in quasi-2D RP systems.

In this work, we introduce an ultrathin poly(vinylidene fluoride) (PVDF) interlayer at the buried PEDOT:PSS/perovskite interface to modulate the crystallization of $BA_2MA_3Pb_4I_{13}$ films. The molecular formula of PVDF is $-(C_2H_2F_2)_n-$, and the chemical structures of PEDOT:PSS and PVDF are illustrated in SI Fig. S1a and b. X-ray photoelectron spectroscopy (XPS) confirms the successful deposition of PVDF on PEDOT:PSS. Optical characterization *via* ultraviolet-visible (UV-vis) and photoluminescence (PL) spectroscopy reveals that the PVDF interlayer effectively suppresses the formation of small-n phases ($n < 4$), which are known to hinder charge transport. Furthermore, grazing-incidence wide-angle X-ray scattering (GIWAXS) and cross-sectional scanning electron microscopy (SEM) demonstrates that PVDF promotes enhanced crystallinity and preferential out-of-plane orientation in the 2D perovskite film. Top-view SEM further corroborates these findings, showing that PVDF modification leads to larger perovskite grain sizes and improved film morphology. As a result of these structural and optoelectronic improvements, PVDF-modified 2D RP PSCs employing $BA_2MA_3Pb_4I_{13}$ as the active layer achieve a champion power conversion efficiency (PCE) of 11.03%, representing a 17.47% enhancement compared to control devices without the PVDF interlayer.

Results and discussion

The UV-vis absorption result of PVDF exhibits only a very weak absorption in the 200–300 nm range, while in the visible spectrum (380–760 nm) no noticeable absorption is observed. Consequently, most incident light can pass through the PVDF layer and reach the perovskite. Therefore, the introduction of PVDF does not adversely affect the light absorption of perovskite in the visible region. XPS was employed to verify the deposition of PVDF on the PEDOT:PSS substrate (Fig. 1a). In the pristine PEDOT:PSS sample, no F 1s peak was detected, confirming the absence of fluorine-containing species. However, after spin-coating a PVDF layer onto PEDOT:PSS, a distinct F 1s peak emerged in the XPS spectrum of the PEDOT:PSS/PVDF composite, providing clear evidence of successful PVDF thin-film formation. Furthermore, spectroscopic ellipsometry measurements confirmed the PVDF layer thickness to be

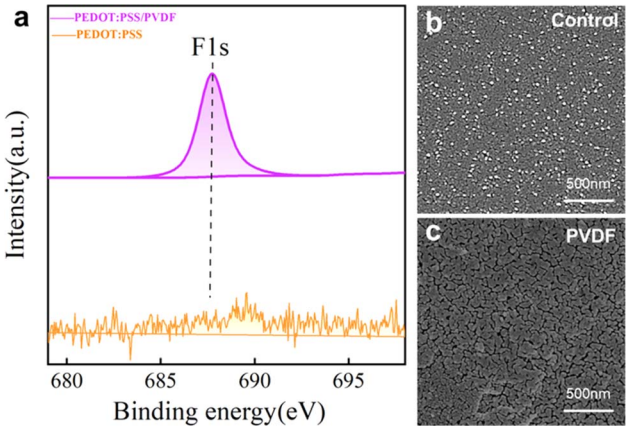

Fig. 1 (a) XPS spectrum of PEDOT:PSS film onto glass and PEDOT:PSS/PVDF film onto glass; (b and c) SEM of perovskite deposited onto PEDOT:PSS and PVDF layer.

1.86 nm. The top and cross-sectional SEM are conducted to investigate the role of PVDF on morphology of the 2D RPP films (Fig. 1b, c) and S1. Compared with the perovskite fabricated onto PEDOT:PSS (hereafter referred to as "control"), the perovskite fabricated onto PVDF modified PEDOT:PSS substrate (here after referred as "PVDF") shows a larger grain size, which indicates the introduce of PVDF could promote the growth of perovskite film. Furthermore, the cross-sectional SEM reveals that some perovskite platelets grown on the PEDOT:PSS substrate exhibit in-plane orientation, whereas those grown on the PVDF-modified PEDOT:PSS substrate show a stronger out-of-plane orientation, which is consistent with the GIWAXS results discussed below. Moreover, the perovskite films grown on the PVDF-modified substrate possess larger grain sizes, with most grains extending continuously from the bottom to the top of the film.

To further investigate the crystallization behavior and orientation of the fabricated 2D perovskite films, GIWAXS measurements were performed (Fig. 2). Both the control film and the PVDF-modified film exhibit spot-like diffraction patterns (Fig. 2a and b), indicating high crystallinity and preferential crystallographic orientation.[19] In the low q region ($q < 1$ $Å^{-1}$), the GIWAXS patterns correspond to small-n phases ($n < 4$).[20] The intensity of these diffraction features is significantly suppressed in the perovskite film deposited on the PEDOT:PSS/PVDF substrate (Fig. 2b), suggesting a reduced presence of small-n phases. Otherwise, the perovskite film on PEDOT:PSS/PVDF exhibits stronger diffraction intensity in the $q \geq 10$ nm^{-1} region (Fig. 2c), indicative of enhanced crystallinity.[21] The out-of-plane orientation of the perovskite films was further analyzed by examining the azimuthal angular distribution of the primary diffraction peak at $q \approx 1$ $Å^{-1}$ (Fig. 2d).[22] Both films display a characteristic dominant peak at 90°, which indicates a preferential out-of-plane orientation relative to the substrate. However, the perovskite film on PEDOT:PSS/PVDF shows a more pronounced azimuthal intensity distribution, suggesting improved crystallographic alignment along the out-of-plane direction on PEDOT:PSS/PVDF.[23] The fluorine atoms in PVDF

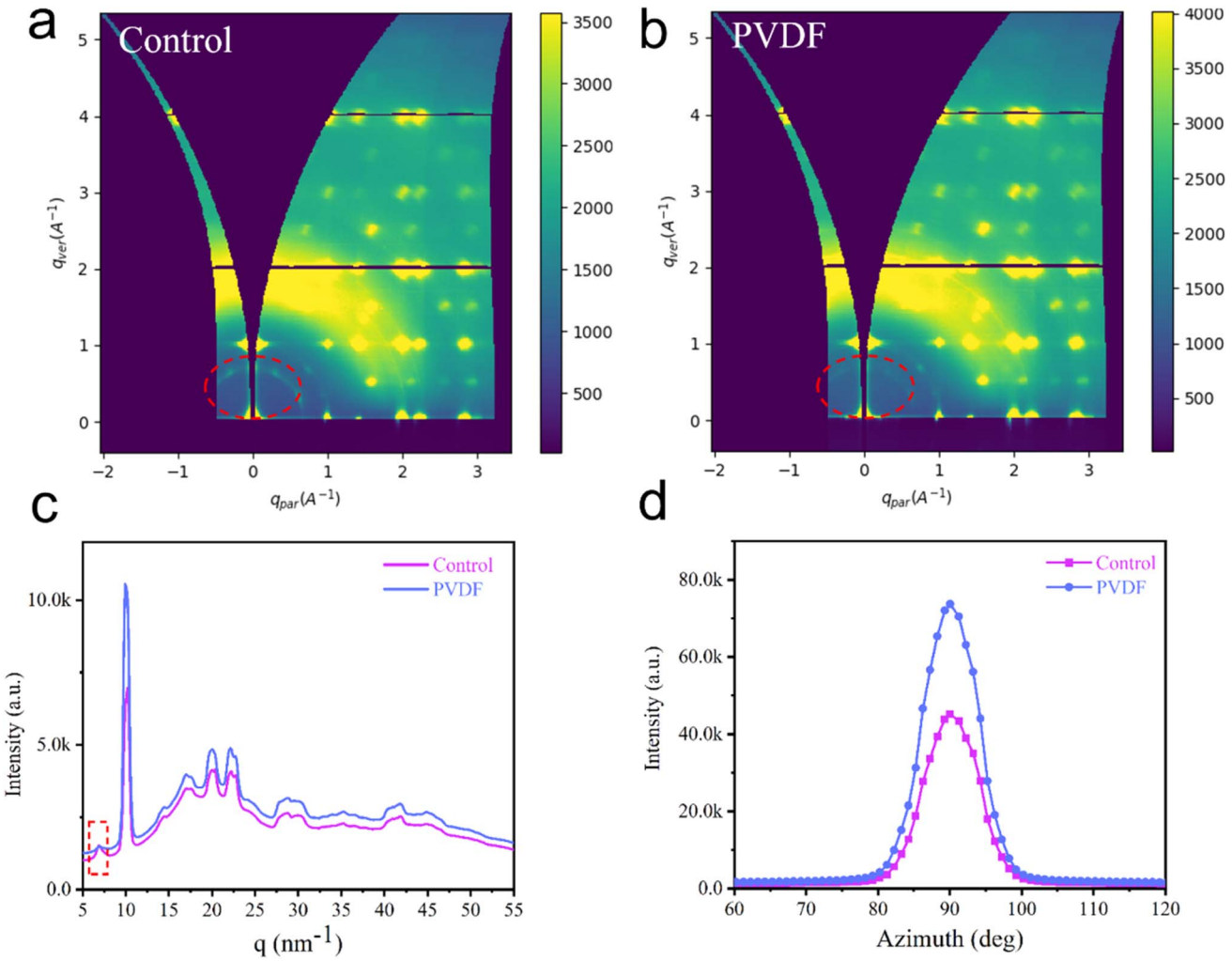

Fig. 2 Grazing-incidence wide-angle X-ray scattering (GIWAXS) images of 2D RPP film fabricated onto (a) PEDOT:PSS, (b) PEDOT:PSS/PVDF. (c) Intensity *versus* q for both perovskite samples. (d) Azimuth angle of the (111) peak for both perovskite samples.

are able to form N–H···F hydrogen bonds with organic cations (MA/FA/BA) and coordinate with under-coordinated Pb^{2+} ions, thereby modulating the nucleation and growth process during film formation (Fig. S3).[24,25] These specific chemical interactions retard rapid crystallization, resulting in larger grain sizes, enhanced out-of-plane orientation, which might contribute to reduce trap-state density and lead to suppressed non-radiative recombination.[24]

The UV-vis absorption spectra were analyzed to evaluate the effect of PVDF on the phase composition of 2D RPP films. Despite we prepared the perovskite precursor solution with a nominal stoichiometric ratio of $n = 4$ ($BA_2MA_3Pb_4I_{13}$), the resulting 2D perovskite films exhibit multiple excitonic absorption features,[5,26] indicating the coexistence of mixed-phase components (Fig. 3a). Distinct absorption peaks are observed at 572 nm, 604 nm, 640 nm, and 740 nm, corresponding to the quantum-confined phases of $n = 2$, $n = 3$, $n = 4$, and the $n = \infty$ (3D-like) phase, respectively.[27,28] Notably, when the 2D perovskite film is deposited on PVDF-modified PEDOT:PSS, the absorption intensity of $n < 4$ phases decrease. This confirms that PVDF suppresses the formation of small-n phases, in agreement with the GIWAXS results. The reduction in small-n phase impurities implies improved phase purity in perovskites grown on PVDF, which may contribute to a more uniform energy landscape and reduce energy or charge-transfer losses.[29]

To probe the spatial distribution of phase components, we performed PL spectroscopy measurements with excitation from both the perovskite side (front illumination) and the substrate side (back illumination) (Fig. 3b). For control, the PL spectra exhibit distinct emission peaks at 619 nm, 649 nm, and 760 nm, corresponding to the $n = 3$, $n = 4$, and $n = \infty$ (3D-like) phases, respectively.[30] There is a 2 nm red-shift for PL of PVDF sample, which could be ascribed to the decrease of small-n phases. A comparative analysis of the front- and back-illuminated PL spectra reveals significant differences in phase distribution. For both perovskite films, back illumination yields stronger PL intensity from the $n = 3$ and $n = 4$ phases compared to front illumination. This observation indicates a vertical phase segregation, where phases of $n = 3$ and $n = 4$ predominantly

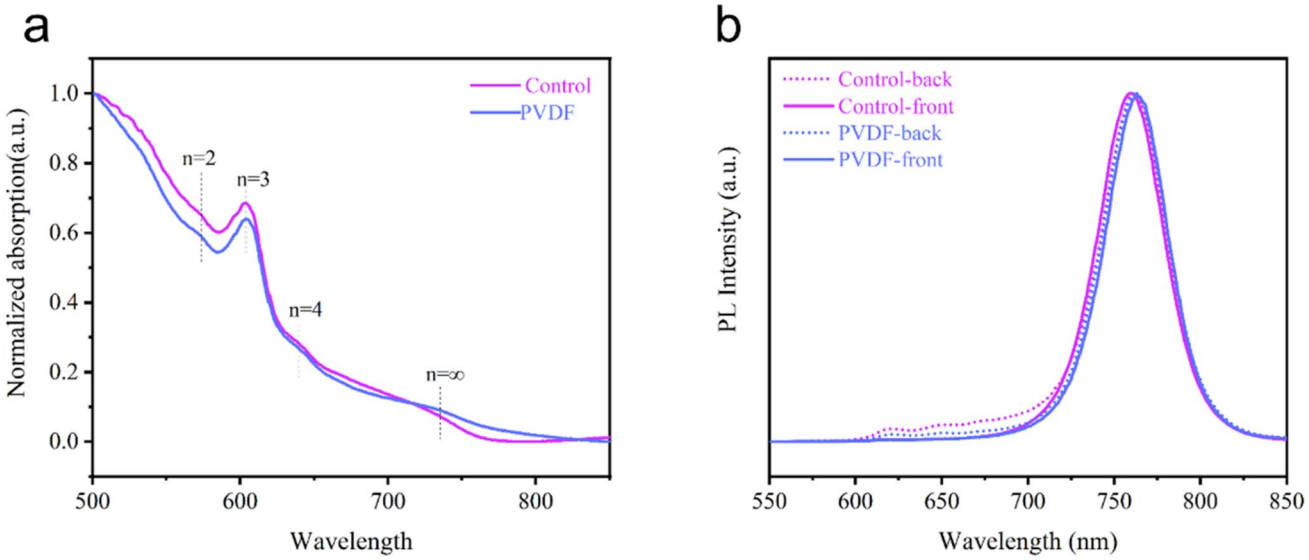

Fig. 3 (a) UV-vis absorption spectrum of perovskite film fabricated onto different substrate. (b) PL of perovskite film fabricated onto different substrate.

accumulate near the substrate interface, while the 3D-like ($n = \infty$) phase concentrates toward the film surface.[31] Such vertical phase gradation is particularly advantageous for charge transport in photovoltaic devices, as it establishes a natural energy alignment that promotes efficient hole transfer from the perovskite layer to the underlying hole transport layer (HTL).[18]

Based on the above discussion, we fabricated 2D PSCs with a configuration of ITO/(PEDOT:PSS/PVDF)/$BA_2MA_3Pb_4I_{13}$/$PC_{61}BM$/BCP/Ag (Fig. 4a) to investigate the effect of PVDF on the device performance. The current density–voltage (J–V) curves under standard AM 1.5 G illumination (Fig. 4b) shows increased open-circuit voltage (V_{OC}) and short-circuit current density (J_{SC}) when inserting a PVDF layer. The relevant photovoltaic parameters are summarized in Table 1. The control device achieved a power conversion efficiency (PCE) of 9.39% with a J_{SC} of 13.87 mA cm^{-2}, V_{OC} of 0.94 V, and fill factor (FF) of 0.72. Compared to the PEDOT:PSS device, the PCE of the champion PEDOT:PSS/PVDF device is significantly increased from 9.39% to 11.03%, due to the increasement of J_{SC} (13.87 to 15.72 mA cm^{-2}) and V_{OC} (0.94 to 0.98 V). The GIWAXS analysis reveals that PVDF incorporation promotes crystalline while suppressing phase heterogeneity in 2D RPP films, which contributes to the observed enhancement in J_{SC}. It's reported low-n phases (*e.g.*, $n = 3$) will act as hole traps in perovskite systems,[5,32] affecting the transporting of carriers.

To evaluate the energy levels of the device, ultraviolet photoelectron spectroscopy (UPS) measurements were performed for PEDOT:PSS, PVDF/PEDOT:PSS, and the 2D RPP film. For PEDOT:PSS deposited on ITO glass, the onset energy (E_i) and cutoff energy ($E_{cut\text{-}off}$) were determined to be 1.75 eV and 18.20 eV, respectively. For PVDF/PEDOT:PSS on ITO glass, the E_i and $E_{cut\text{-}off}$ values were 1.97 eV and 18.22 eV, respectively. Based on these results, the corresponding work functions were calculated as 4.77 eV and 4.97 eV using the equation $\varphi = 21.22 - (E_{cut\text{-}off} - E_i)$ (Fig. 5a and b). For the 2D RPP film, the $E_{cut\text{-}off}$, E_i, and valence band minimum were determined to be 17.80 eV, 2.12 eV, and 0.10 eV, respectively (SI Fig. S5a–c). By combining these with the optical bandgap of 1.62 eV for the 2D RPP film obtained from Tauc plots (SI Fig. S4), the conduction band and valence band positions were estimated to be 4.01 eV and 5.63 eV, respectively (Fig. S5c). The overall energy level diagram of the device is presented in Fig. 5c. Notably, the introduction of PVDF reduces the hole extraction barrier from 0.86 eV to 0.66 eV, thereby facilitating more efficient hole extraction.

To further elucidate the charge transport dynamics of perovskite film with/without PVDF, we performed time-resolved photoluminescence (TRPL) measurements under substrate-side excitation (Fig. 6). Biexponential fitting of the decay curves (Table 2) demonstrates that PVDF-modified films exhibit a shorter carrier lifetime (2.02 ns) compared to the control sample (2.89 ns), suggesting more efficient charge transport and extraction processes.[33,34] Furthermore, the increased grain size observed in PVDF-incorporated films reduces grain boundary density, thereby suppressing non-radiative recombination pathways. These collective effects contribute to improved V_{OC}.[35] To evaluate the producibility of the results, we analyzed the statistical data of V_{OC}, J_{SC}, FF, and PCE of 6 devices from the same batch, as shown in Fig. 4c–f. The relevant photovoltaic parameters are also listed in Table 1. The average V_{OC}, J_{SC}, FF, and PCE show a consistent increasing tendency with that of the champion device (Fig. 6).

Finally, we tested the stability of devices with and without PVDF under dark conditions in air (SI Fig. S6). The results show that the control device retained only 63% of its initial efficiency after 410 hours, whereas the device incorporating PVDF retained 67% of its initial efficiency after the same duration. These results indicate that the introduction of PVDF contributes to enhanced device stability. Although the improvement is

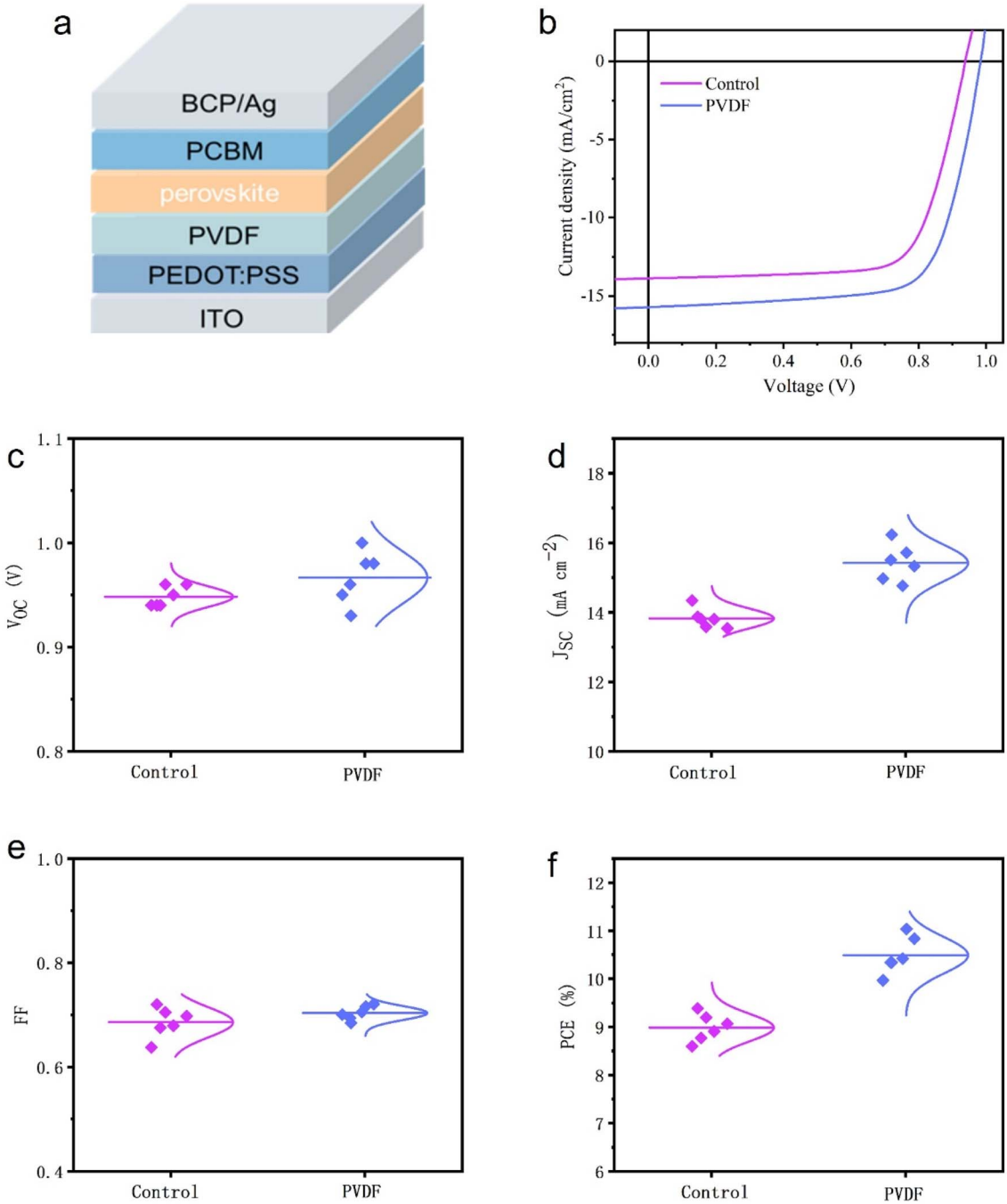

Fig. 4 (a) Perovskite solar cell architecture. (b) Solar cell J–V curves from forward scan. (c–f) Statistic parameters of V_{OC}, J_{SC}, FF and PCE of the 6 devices form the same batch.

Table 1 A summary of the solar cell parameters

Device	J_{SC}/mA cm^2	V_{OC}/V	FF	PCE/%
Control	13.87 (13.823 ± 0.2873)	0.94 (0.948 ± 0.0098)	0.72 (0.686 ± 0.0288)	9.39 (8.989 ± 0.2889)
PVDF	15.72 (15.421 ± 0.5298)	0.98 (0.967 ± 0.0251)	0.72 (0.7038 ± 0.0135)	11.03 (10.489 ± 0.3837)

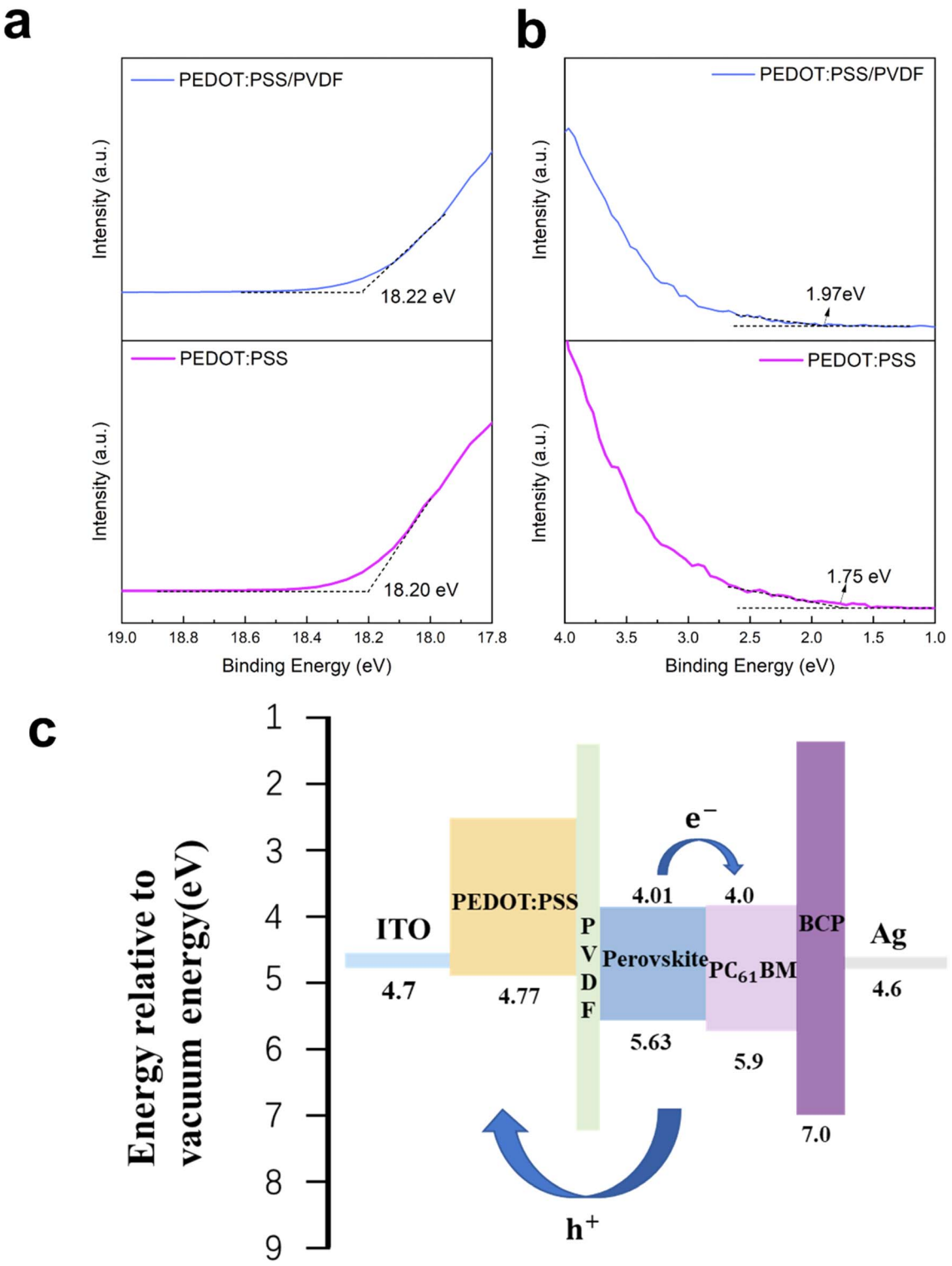

Fig. 5 (a) UPS of PEDOT:PSS and PVDF/PEDOT:PSS in the (a) cutoff ($E_{cut\text{-}off}$) and (b) onset (E_i), (c) schematic energy level diagram of the entire device without or with PVDF interlayer.

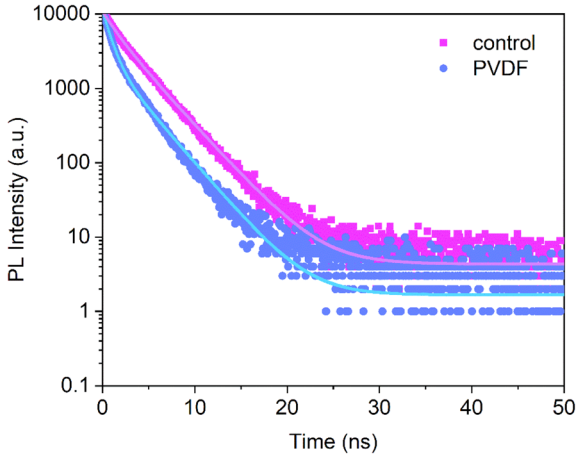

Fig. 6 TRPL spectra of 2D RPP films on PEDOT:PSS and PEDOT:PSS/PVDF substrates.

Table 2 Parameters of the TRPL spectroscopy of control film and PVDF modified film with a structure of ITO/PEDOT:PSS/PVDF/perovskite. The excitation wavelength for TRPL was 485 nm. The average lifetime (τ_{ave}) is calculated using: $\tau_{ave} = (A_1\tau_1^2 + A_2\tau_1^2)/(A_1\tau_1 + A_2\tau_2)$

Sample	A_1	τ_1	A_2	τ_2	τ_{ave}
Control	3450.25	1.34	7259.37	3.20	2.89 ns
PEDOT:PSS/PVDF	8388.01	0.83	2785.91	3.01	2.02 ns

modest, it still demonstrates the positive role of PVDF in suppressing degradation and prolonging device lifetime.

Conclusion

In summary, we have demonstrated that a simple PVDF interfacial modification strategy can effectively regulate the phase distribution and crystallization behavior of 2D RP perovskite films. The ultra-thin PVDF interlayer not only suppresses the formation of undesirable low-*n* phases but also promotes favorable vertical orientation and enhances crystallinity in $BA_2MA_3Pb_4I_{13}$ perovskite films. These synergistic effects contribute to improved charge transport and collection efficiency in the resulting devices. The significant performance enhancement (17.47%) achieved through this approach highlights the critical role of buried interface engineering in optimizing 2D perovskite solar cells. This work provides a facile yet effective strategy for controlling phase purity and crystal orientation in low-dimensional perovskite photovoltaics, offering new insights for the development of high-performance PSCs.

Experimental details

Material

All chemicals were used as received without further purification. Lead iodide (PbI_2) was purchased from Advanced Election Technology Co., Ltd. Methylammonium iodide (MAI) and butylammonium iodide (BAI) were obtained from Xi'an Polymer Light Technology Corp. The hole-transporting layer material, poly(3,4-ethylenedioxythiophene):polystyrene sulfonate (PEDOT:PSS, Clevios™ AI 4083), was acquired from Heraeus. The electron transport materials,[6,6]-phenyl-C_{61}-butyric acid methyl ester ($PC_{61}BM$) and bathocuproine (BCP), were purchased from Xi'an Polymer Light Technology Corp. Polyvinylidene fluoride (PVDF), *N*,*N*-dimethylformamide (DMF), and chlorobenzene (CB) were sourced from Sigma-Aldrich. The $BA_2MA_3Pb_4I_{13}$ precursor solution was prepared by mixing PbI_2, MAI, and BAI in a molar ratio of 4 : 3 : 2 in DMF solvent, yielding a final concentration of 0.25 mol L^{-1}. The $PC_{61}BM$ solution was prepared by dissolving in CB at a concentration of 25 mg mL^{-1}.

Device fabrication

The indium tin oxide (ITO)-coated glass substrates, with a sheet resistance of 15 Ω $\square^{-1}$, were sequentially cleaned by ultrasonication in glass detergent, deionized water, and ethanol. After drying with a nitrogen gun, the substrates underwent oxygen plasma treatment for 10 min to enhance surface cleanliness. The HTL was prepared by spin-coating filtered PEDOT:PSS (Clevios™ AI 4083) onto the ITO substrates at 4000 rpm for 40 s, followed by thermal annealing at 120 °C for 15 min in ambient air. For devices incorporating a PVDF interlayer, a PVDF solution was spin-coated on the PEDOT:PSS at 4000 rpm for 20 s and annealed at 100 °C for 10 min. All substrates were then transferred into a nitrogen-filled glovebox for subsequent processing. Prior to perovskite deposition, the substrates were preheated at 100 °C for 10 min. The $BA_2MA_3Pb_4I_{13}$ precursor solution (0.25 M in DMF) was then spin-coated at 5000 rpm for 20 s onto either PEDOT:PSS or PEDOT:PSS/PVDF, followed by thermal annealing at 100 °C for 10 min to form the perovskite active layer. For the electron-transport layer (ETL), a $PC_{61}BM$ solution (25 mg mL^{-1} in chlorobenzene) was spin-coated at 1500 rpm for 40 s. Subsequently, an ~8 nm-thick bathocuproine (BCP) buffer layer was deposited *via* thermal evaporation. Finally, a 100 nm silver (Ag) cathode was thermally evaporated under high vacuum (5×10^{-4} Pa) to complete the device structure. The active area of each device, defined by the overlap between the Ag cathode and ITO anode, was 4 mm^2.

Device characterization

Film thicknesses were determined using spectroscopic ellipsometry. The *J*–*V* characteristics of the PSCs were measured under simulated AM 1.5 G solar irradiation (100 mW cm^{-2}) using a Keithley 2400 source measurement unit. Surface morphology was analyzed by scanning electron microscopy (SEM, Sigma 300, Carl Zeiss, Germany). Grazing-incidence wide-angle X-ray scattering (GIWAXS) measurements were conducted at the Soft Matter Interfaces beamline (12-ID) of the National Synchrotron Light Source II (NSLS-II) at Brookhaven National Laboratory. XPS and UPS measurements were performed using a Thermo ESCALAB 250Xi system. Optical properties were evaluated by UV-vis-NIR spectroscopy (a Cary 5000) on devices with the structure of ITO/PEDOT:PSS/PVDF/perovskite, with illumination incident from the perovskite side. Steady-state PL

spectra were acquired using a Horiba QuantaMaster-8075-21 spectrophotometer on samples with the architecture of ITO/PEDOT:PSS/(PVDF)/perovskite, employing an excitation wavelength of 550 nm. Time-resolved photoluminescence (TRPL) measurements were conducted with excitation through the ITO side with the architecture of ITO/PEDOT:PSS/(PVDF)/perovskite. All characterizations were performed under ambient atmospheric conditions without device encapsulation.

Conflicts of interest

There are no conflicts to declare.

Data availability

The data that supports the findings of this study are available from the corresponding author (yangllei@gxmzu.edu.cn).

Supplementary information is available. See DOI: https://doi.org/10.1039/d5ra06360d.

Acknowledgements

This work is supported by the Young and Middle-aged Teachers Basic Ability Improvement Project of Guangxi Department of Education (2024KY0179), the Guangxi Natural Science Foundation (2025GXNSFBA069208), the National Natural Science Foundation of China (62465003), the Scientific Research Initiation Project for Recruited Talent at Guangxi Minzu University (2023KJQD01), the Scientific Research Start-Up Funding under the 2024 First Batch Universal Support Policy for Young Talents (301780212), the Guangxi Young Elite Scientist Sponsorship Program (GXYESS2025155), the National College Students Innovation and Entrepreneurship Training program (S202310608056). The authors also thank Dr Yugang Zhang from Brookhaven National Laboratory for the GIWAXS measurement, and PhD candidate Jingjing Zhao and Xin Li from Guangxi University for the thickness and UV-vis measurement. We also thank Yuhao Jiang for his assistance with the preparation of the diagrams.

References

1 P. Liu, X. Li, T. Cai, W. Xing, N. Yang, H. Arandiyan, Z. Shao, S. Wang and S. Liu, Molecular Structure Tailoring of Organic Spacers for High-Performance Ruddlesden-Popper Perovskite Solar Cells, *Nano-Micro Lett.*, 2024, **17**(1), 35.

2 C. Wang, X. Dong and F. Chen, Recent progress of two-dimensional Ruddlesden-Popper perovskites in solar cells, *Mater. Chem. Front.*, 2023, **7**(22), 5786–5805.

3 Y. Zhang, M. Chen, T. He, H. Chen, Z. Zhang, H. Wang, H. Lu, Q. Ling, Z. Hu and Y. Liu, Highly Efficient and Stable FA-Based Quasi-2D Ruddlesden-Popper Perovskite Solar Cells by the Incorporation of β-Fluorophenylethanamine Cations, *Adv. Mater.*, 2023, e2210836.

4 J. Kong, Y. Shin, J. A. Rhr, H. Wang and A. D. Taylor, CO2 doping of organic interlayers for perovskite solar cells, *Nature*, 2021, **594**(7861), 51–56.

5 J. Meng, D. Song, D. Huang, Y. Li, Y. Li, A. Maqsood, S. Zhao, B. Qiao, H. Zhu and Z. Xu, Enhanced VOC of two-dimensional Ruddlesden–Popper perovskite solar cells using binary synergetic organic spacer cations, *Phys. Chem. Chem. Phys.*, 2020, **22**(1), 54–61.

6 H. Tsai, W. Nie, J.-C. Blancon, C. C. Stoumpos, R. Asadpour, B. Harutyunyan, A. J. Neukirch, R. Verduzco, J. J. Crochet, S. Tretiak, L. Pedesseau, J. Even, M. A. Alam, G. Gupta, J. Lou, P. M. Ajayan, M. J. Bedzyk, M. G. Kanatzidis and A. D. Mohite, High-efficiency two-dimensional Ruddlesden–Popper perovskite solar cells, *Nature*, 2016, **536**(7616), 312–316.

7 C. Liang, H. Gu, Y. Xia, Z. Wang and W. Huang, Two-dimensional Ruddlesden–Popper layered perovskite solar cells based on phase-pure thin films, *Nat. Energy*, 2021, **6**(1), 1–8.

8 N. Liu, P. Liu, H. Zhou, Y. Bai and Q. Chen, Understanding the Defect Properties of Quasi-2D Halide Perovskites for Photovoltaic Applications, *J. Phys. Chem. Lett.*, 2020, **11**(9), 3521–3528.

9 M. Chunqing, L. Ming-Fai and L. Chun-Sing, A simple method for phase control in two-dimensional perovskite solar cells, *J. Mater. Chem. A*, 2018, **6**, 18871–18876.

10 N. Liu, P. Liu, H. Ren, H. Xie and Q. Chen, Probing Phase Distribution in 2D Perovskites for Efficient Device Design, *ACS Appl. Mater. Interfaces*, 2019, **12**(2), 3127–3133.

11 B. Du, Y. Lin, J. Ma, W. Gu, F. Liu, Y. Yao and L. Song, Buried interface management toward high-performance perovskite solar cells, *Chem. Sci.*, 2024, 1876–1884.

12 M. Jiang, X. Zhang and F. Wang, Enabling monodisperse perovskite phase with buried interface modification toward efficient light-emitting diodes, *Nano Res. Energy*, 2023, e9120069.

13 B. Zhou, C. Shang, C. Wang, D. Qu, J. Qiao, X. Zhang, W. Zhao, R. Han, S. Dong, Y. Xue, Y. Ke, F. Ye, X. Yang, Y. Tu and W. Huang, Strain Engineering and Halogen Compensation of Buried Interface in Polycrystalline Halide Perovskites, *Research*, 2024, **7**, 0309.

14 J. Dong, D. Song, J. Meng, Y. Lu, Y. Li, B. Qiao, S. Zhao and Z. Xu, Interface energy level alignment and improved film quality with a hydrophilic polymer interlayer to improve the device efficiency and stability of all-inorganic halide perovskite light-emitting diodes, *J. Mater. Chem. C*, 2020, **8**, 6743–6748.

15 J. Meng, J. A. Rhr, H. Wang, B. E. Sartor, D. Song, A. Katzenberg, M. A. Modestino, Z. Xu, J. Kong and A. D. Taylor, A compact electron transport layer using a heated tin-oxide colloidal solution for efficient perovskite solar cells, *Sol. RRL*, 2021, 2100794.

16 Z. Liu, L. Wang, C. Xu, X. Xie and Y. Zhang, Hole-Transport-Underlayer-Induced Crystallization Management of Two-Dimensional Perovskites for High-Performance Inverted Solar Cells, *ACS Appl. Energy Mater.*, 2021, **4**(10), 10574–10583.

17 S. Tian, J. Chen, X. Lian, Y. Wang, Y. Zhang, W. Yang, G. Wu, W. Qiu and H. Chen, Engineering the underlying surface to manipulate the growth of 2D perovskites for highly efficient solar cells, *J. Mater. Chem. A*, 2019, **7**(23), 14027–14032.

18 T. Liu, Y. Jiang, M. Qin, J. Liu, L. Sun, F. Qin, L. Hu, S. Xiong, X. Jiang and F. Jiang, Tailoring vertical phase distribution of quasi-two-dimensional perovskite films via surface modification of hole-transporting layer, *Nat. Commun.*, 2019, **10**(1), 878.

19 Y. Chen, N. Yang, G. Zheng, F. Pei, W. Zhou, Y. Zhang, L. Li, Z. Huang, G. Liu, R. Yin, H. Zhou, C. Zhu, T. Song, C. Hu, D. Zheng, Y. Bai, Y. Duan, Y. Ye, Y. Wu and Q. Chen, Nuclei engineering for even halide distribution in stable perovskite/silicon tandem solar cells, *Science*, 2024, **385**(6708), 554–560.

20 H. Wang, Y. Pan, X. Li, Z. Shi, X. Zhang, T. Shen, Y. Tang, W. Fan, Y. Zhang, F. Liu, Y. Wang, K. Liu, Y. Wang, C. Li, T. Hu, L. Deng, J. Wang, A. Yu, H. Dong, Y. Yang, L. Xue, L. Shi and Y. Zhan, Band Alignment Boosts over 17% Efficiency Quasi-2D Perovskite Solar Cells via Bottom-Side Phase Manipulation, *ACS Energy Lett.*, 2022, **7**(10), 3187–3196.

21 Y. S. Tingare, C. H. Lin, C. Su, S. C. Chou, Y. C. Hsu, D. Ghosh, N. W. Lai, X. R. Lew, S. Tretiak and H. Tsai, Ionization of hole-transporting materials as a method for improving the photovoltaic performance of perovskite solar cells, *J. Mater. Chem. A*, 2024, **12**(4), 11.

22 P. Cheng, P. Wang, Z. Xu, X. Jia and S. F. Liu, Ligand-Size Related Dimensionality Control in Metal Halide Perovskites, *ACS Energy Lett.*, 2019, **4**(8), 1830–1838.

23 D. Li, X. Sun, Y. Zhang, Z. Guan, Y. Yue, Q. Wang, L. Zhao, F. Liu, J. Wei and H. Li, Uniaxial-Oriented Perovskite Films with Controllable Orientation, *Adv. Sci.*, 2024, **11**(19), 2401184.

24 R. Sun, Q. Tian, M. Li, H. Wang, J. Chang, W. Xu, Z. Li, Y. Pan, F. Wang and T. Qin, Over 24% efficient poly (vinylidene fluoride)(PVDF)-coordinated perovskite solar cells with a photovoltage up to 1.22 V, *Adv. Funct. Mater.*, 2023, **33**(6), 2210071.

25 A. Shit, P. Chal, S. Mondal and A. K. Nandi, Influence of Poly(Vinylidene fluoride) on photovoltaic performance of interfacially engineered band gap modulated P3TAA-co-P3HT perovskite solar cell at ambient condition, *Polymer*, 2019, **185**, 121973.

26 X. Gan, K. Li, L. Du, R. Wang, Y. Chang, L. Guo and H. Liu, High-Quality Thiophene-Based Two-Dimensional Perovskite Films Prepared with Dual Additives and Their Application in Solar Cells, *ACS Omega*, 2024, **9**(46), 46006–46016.

27 K. Wang, Z. Y. Lin, Z. Zhang, L. Jin, K. Ma, A. H. Coffey, H. R. Atapattu, Y. Gao, J. Y. Park and Z. Wei, Suppressing phase disproportionation in quasi-2D perovskite light-emitting diodes, *Nat. Commun.*, 2023, 397.

28 E. Klein, A. Black, Z. Tokmak, C. Strelow and C. Klinke, Micron-Size Two-Dimensional Methylammonium Lead Halide Perovskites, *ACS Nano*, 2019, **13**(6), 6955–6962.

29 Y. Yang, S. Feng, W. Xu, M. Li, L. Li, X. Zhang, G. Ji, X. Zhang, Z. K. Wang and Y. Xiong, Enhanced Crystalline Phase Purity of CH3NH3PbI3-xClx Film for High Efficiency Hysteresis-free Perovskite Solar Cells, *ACS Appl. Mater. Interfaces*, 2017, **9**(27), 23141–23151.

30 J. Liu, J. Leng, K. Wu, J. Zhang and S. Jin, Observation of Internal Photoinduced Electron and Hole Separation in Hybrid Two-Dimensional Perovskite Films, *J. Am. Chem. Soc.*, 2017, 1432–1435.

31 Y. Li, H. Li, L. Tian, Q. Wang, F. Wu, F. Zhang, L. Du and Y. Huang, Vertical phase segregation suppression for efficient FA-based quasi-2D perovskite solar cells via HCl additive, *J. Mater. Sci.: Mater. Electron.*, 2020, **31**(15), 12301–12308.

32 X. Zhang, R. Munir, Z. Xu, Y. Liu, H. Tsai, W. Nie, J. Li, T. Niu, D. M. Smilgies and M. G. Kanatzidis, Phase Transition Control for High Performance Ruddlesden-Popper Perovskite Solar Cells, *Adv. Mater.*, 2018, **21**, 1707166.

33 Z. Wang, D. P. Mcmeekin, N. Sakai, S. V. Reenen, K. Wojciechowski, J. B. Patel, M. B. Johnston and H. J. Snaith, Efficient and air-stable mixed-cation lead mixed-halide perovskite solar cells with n-doped organic electron extraction layers, *Adv. Mater.*, 2017, (5), 201604186.

34 H. Tan, A. Jain, O. Voznyy, X. Lan and E. H. Sargent, Efficient and stable solution-processed planar perovskite solar cells via contact passivation, *Science*, 2017, **355**(6326), 722–726.

35 D. Huang, T. Goh, J. Kong, Y. Zheng, S. Zhao, Z. Xu and A. D. Taylor, Perovskite solar cells with a DMSO-treated PEDOT:PSS hole transport layer exhibit higher photovoltaic performance and enhanced durability, *Nanoscale*, 2017, **9**, 4236–4243.